External cavity mode structure of a two-mode VCSEL subject to optical feedback

K. Green, [a] B. Krauskopf, [b,a] D. Lenstra [c]

[a] *Department of Theoretical Physics, Faculty of Exact Sciences, Vrije Universiteit, De Boelelaan 1081, 1081 HV Amsterdam, The Netherlands*

[b] *Department of Engineering Mathematics, University of Bristol, Queen's Building, University Walk, Bristol BS8 1TR, UK*

[c] *Faculty of Electrical Engineering, Mathematics and Computer Science, Delft University of Technology, Mekelweg 4, 2628 CD Delft, The Netherlands*

Abstract

We consider a multi-transverse-mode vertical-cavity surface-emitting laser (VCSEL) subject to optical feedback. The system is modeled by a partial differential equation for the spatial carrier population, which is coupled to delay differential equations for the electric fields of the participating transverse modes that are subject to external optical feedback. We consider here the case that the VCSEL supports the two basic, rotationally symmetric, linearly polarized optical modes LP_{01} and LP_{02}. In our model each LP mode receives feedback not only from itself but also from the other LP mode; the amount of cross-feedback can be controlled by a parameter.

Specifically, we use numerical continuation techniques to present a detailed analysis of the steady state, external cavity mode (ECM) structure in dependence on the feedback strength, the feedback phase and the amount of cross-feedback. This shows that the case of zero cross-feedback is degenerate and changes quite dramatically even in the presence of small feedback from the other transverse mode. On the other hand, in an intermediate range of cross-feedback the ECM structure does not change qualitatively in a physically relevant range of feedback strength. We consider the entire transition from zero cross-feedback to zero self-feedback, in which we identify the key changes in the ECM structure.

Key words: VCSEL; delayed partial differential equation; numerical continuation; multi-transverse-mode operation; multistability

1 Introduction

Vertical-cavity surface-emitting lasers (VCSELs) have received a lot of attention recently due to their desirable properties in a number of applications. A key advantage is that VCSELs only require an applied current of a few microamperes in order to lase. Furthermore, they are cheap to mass produce and can be tested 'on-wafer', in large arrays. These properties make VCSELs popular in applications, such as, on-chip or chip-to-chip optical interconnects [13]. Moreover, due to their cylindrical geometry, VCSELs emit a cylindrical beam of light. Therefore, they can easily be coupled to optical fibers, so that they are ideally suited for applications in optical telecommunication.

A short optical cavity means that VCSELs provide single longitudinal-mode operation. On the other hand, depending on the size of its aperture diameter (typically in the range of 10 to 150 microns), a VCSEL can support a number of transverse optical modes. While a larger aperture provides a higher gain area in the VCSEL and subsequent higher output intensity of the light, this advantage is balanced against an increasing multi-transverse-mode operation as the aperture diameter is increased; see, for example, Ref. [24].

Theoretically, spatially-dependent VCSEL models fall into two categories [15]. For gain-guided VCSELs, the optical (electric) field profile is fully determined by the spatial carrier distribution, and vice versa. Thus, one uses a partial differential equation (PDE) description for both the electric field and the inversion. Alternatively, in weakly index-guided VCSELs, the electric field profiles are determined by the geometry of the VCSEL, which is a cylindrical dielectric waveguide. In this case the electric field is described by an ordinary differential equation (ODE), which is coupled to a PDE describing the spatial carrier distribution (subject to carrier diffusion). More specifically, the transverse mode characteristics of the VCSEL are investigated by using linearly polarized (LP) modes; one speaks of the *modal description* of the VCSEL. For a weakly guiding cylindrical waveguide, the LP modes approximate the complete set of optical modes, that is, the transverse electric (TE), transverse magnetic (TM) and hybrid modes [24].

In this paper we consider the influence of optical feedback on the transverse modes of a VCSEL as modeled in the framework of the spatially-extended modal description. We restrict our attention to the case of a VCSEL that lases in a fixed polarization throughout its operating range. (An alternative approach is to model the vector nature of the laser field, taking into account two circularly polarized emission states; see, for example, Ref. [15].) The inclusion of optical feedback leads to a description of the optical fields of the involved transverse modes by delay differential equations (DDEs). Hence, in conjunction with the equation for the spatial carrier distribution one is dealing

with a mathematically sophisticated model in the form of a delayed partial differential equation (DPDE). Spatially-extended, modal models of a VCSEL subject to optical feedback have been introduced and investigated in quite some detail over the past decade. Importantly, a key modeling assumption of previous work has always been that the electric field of a given transverse mode receives *feedback only from itself*. Valle et al. introduce the modal description and show (by means of numerical simulations) the dynamic evolution of competing transverse modes in Refs. [20,21]; the transient, 'turn-on' dynamics of the VCSEL are also investigated. Law and Agrawal [10,12] use numerical integration to identify period-doubling and quasiperiodic routes to chaos in VCSELs under single-mode and two-mode operation, where they consider azimuthally symmetric optical modes (an approximation, used to model a combination of higher-order LP modes). Furthermore, they investigate the effect of a modulated current in Ref. [11]. Torre and co-workers [18] investigate the transverse dynamics of a similar VCSEL model, again with feedback such that the electric field of each transverse mode only influences itself. Likewise, a modulated current is considered in Ref. [19].

We are interested in the influence of cross-feedback from one transverse mode to the other – an effect that has not been included in the modeling literature so far. To this end, we consider the case that the VCSEL supports only two transverse modes, namely the two basic LP_{01} and LP_{02} modes [18]. In our model, introduced fully in Sec. 3, each LP mode receives feedback not only from itself but also from the other LP mode. We introduce a general setup where the total feedback is governed by the feedback strength and the feedback phase, and the relative amount of self/cross-feedback is determined by a homotopy parameter. This allows us to study how the behavior of the system changes when the total feedback is fixed, but the relative amount of cross-feedback is increased from zero (the zero cross-feedback case is considered in the above references).

Specifically, we present a detailed bifurcation analysis of the external cavity mode (ECM) structure in dependence on the feedback strength, the feedback phase and the amount of cross-feedback. The ECMs are the basic solutions of the system, characterized by a fixed intensity of lasing at a fixed frequency with a fixed spatial carrier profile. In other words, they are continuous-wave (CW) solutions. The overall ECM structure is important because it underpins the more complicated dynamics. For example, Hopf bifurcations give rise to periodic output, which in turn may become chaotic. As is well known from the COF laser, chaotic dynamics may involve close visits to unstable ECMs of saddle type [22]. Indeed, a detailed analysis of the dependence of the ECMs on relevant parameters is needed as a basis for a full understanding of the VCSEL model with optical feedback.

Our results show that the case of zero cross-feedback is very special (not

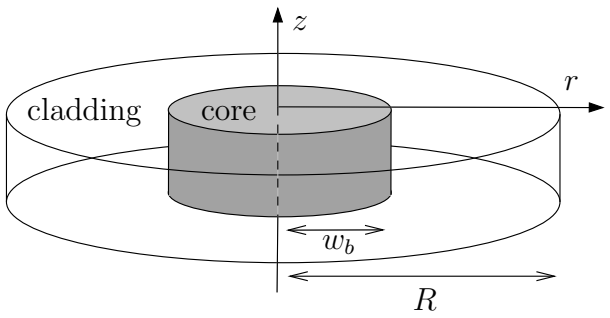

Fig. 1. The geometry of the VCSEL with a cylindrical waveguide.

generic) and changes quite dramatically even in the presence of small feedback from the other LP mode. On the other hand, through to an intermediate range of cross-feedback the ECM structure does not change qualitatively in a physically relevant range of feedback strength. We consider the entire transition from zero cross-feedback to zero self-feedback, and we identify the relevant changes (bifurcations) of the ECM structure. In particular, we also compute regions of stability on branches of ECMs.

Even the seemingly quite simple situation of a VCSEL model with only two LP modes and optical feedback is mathematically very challenging. Indeed, the bifurcation analysis of a DPDE of this sort requires the use of advanced computational tools. In particular, the computation of stability in such infinite-dimensional systems is not a simple matter. We employ here the technique of numerical continuation of ECMs, through the use of the package DDE-BIFTOOL [1] for the numerical bifurcation analysis of DDEs; see Sec. 3.1 for more details. Numerical continuation has been used with great success in analyzing small sized systems of (three to six) DDEs modeling specific lasers with feedback, including lasers with COF [5] and filtered optical feedback (FOF) [2,4], two mutually delay-coupled lasers [3], and two coupled polarization modes of a non-spatial, transversely single-mode VCSEL [17]; see also the survey [8]. However, the technique has rarely been used to analyze a system as large as that considered here. Namely, the discretization of the PDE for the carrier diffusion leads to a system of 105 coupled DDEs. In this respect, the study presented here can also be seen as a demonstration of the efficiency of numerical tools for the bifurcation analysis of systems described by PDEs subject to delay.

This paper is organized as follows. A brief derivation of the LP modes is given in Sec. 2. In Sec. 3 we introduce the dimensionless rate equations describing a VCSEL and our general form of optical feedback. The basic ECM structure is identified in Sec. 4, while Secs. 5 and 6 examine changes in the ECM structure and ECM stability as feedback parameters are varied. We draw some conclusions and discuss future work in Sec. 7.

2 The linearly polarized modes

Key to our study is the multi-transverse-mode operation of the VCSEL. In this section, we briefly summarize how one obtains the linearly polarized (LP_{mn}) modes; for more details we refer to Refs. [20] and [24]. The modal profiles ψ_{mn} describe the LP_{mn} modes found in a weakly guided cylindrical dielectric waveguide (the cylindrical geometry of the VCSEL); see Fig. 1. To obtain these profiles one starts with the assumption that the electromagnetic fields are plane-waves in the longitudinal direction, z. Thus, Maxwell's equation can be simplified to the following scalar wave equation

$$r^2\frac{\partial^2\psi_{mn}(r,\phi)}{\partial r^2}+r\frac{\partial\psi_{mn}(r,\phi)}{\partial r}+\frac{\partial^2\psi_{mn}(r,\phi)}{\partial\phi^2}+r^2\frac{q_n^2}{w_b^2}\psi_{mn}(r,\phi)=0, \tag{1}$$

where ψ_{mn} represents the longitudinal component of the optical field, w_b is the radius of the active region of the VCSEL and

$$q_n\equiv\begin{cases}u_n=a\left(\epsilon^{\text{core}}\kappa_n^2-\beta^2\right)^{1/2} & r\le w_b\\ w_n=a\left(\beta^2-\epsilon^{\text{clad}}\kappa_n^2\right)^{1/2} & r>w_b.\end{cases} \tag{2}$$

Here, β is the longitudinal propagation constant, ϵ^{core} and ϵ^{clad} are the dielectric constants for the active (core) and cladding regions of the VCSEL, respectively, and κ_n is the wave-number to be determined.

Secondly, noting the circular symmetry of the VCSEL around the optical axis, the wave equation should satisfy periodic solutions in the azimuthal direction, that is,

$$\psi_{mn}(r,\phi)=\psi_{mn}(r)e^{\pm im\phi}. \tag{3}$$

Therefore, the components (radial, azimuthal and vertical) of the electric and magnetic fields are found as solutions of a scalar wave equation with only a dependence on the radial direction r:

$$r^2\frac{\partial^2\psi_{mn}(r)}{\partial r^2}+r\frac{\partial\psi_{mn}(r)}{\partial r}+\left[r^2q_n\psi_{mn}(r)-m^2\right]=0. \tag{4}$$

Solutions to Eq. (4) are given in terms of Bessel functions of the first kind, J_m, inside the core region ($r\le w_b$) and modified Bessel functions of the second kind, K_m, inside the cladding region ($r>w_b$). Specifically, solutions are of the form

$$\psi_{mn}(r) = \begin{cases} \frac{J_m(u_n r/w_b)}{J_m(u_n)} & r \leq w_b \\ \frac{K_m(w_n r/w_b)}{K_m(w_n)} & r > w_b. \end{cases} \tag{5}$$

The final step in determining ψ_{mn} is to use the condition that at the boundary $r = w_b$, between the core region and the cladding, the tangential components of the field must be continuous. This leads to the eigenvalue problem

$$u_n \frac{J_{m+1}(u_n)}{J_m(u_n)} - w_n \frac{K_{m+1}(w_n)}{K_m(w_n)} = 0, \tag{6}$$

from which u_n and w_n can be determined and, hence, ψ_{mn} can be found.

The magnetic field can be found directly from the electric field [24]. Therefore, as is common in the literature, we consider the electric field as describing the entire optical field.

Finally, we note that the modal profiles ψ_{mn} are rescaled such that

$$\int_0^R \psi_{mn} r dr = 1, \tag{7}$$

where R is the total radius of the device.

3 Two-mode rate equation model

We consider the simplest case of a VCSEL in which only the LP_{01} and LP_{02} modes are excited [18]. We note that the VCSEL may support more, higher-order modes. However, the goal of our study is to show how the ECM structure qualitatively develops in the simplest case, where, in dimensionless form, the rate equation model [20] is given as

$$\frac{dE_k}{dt} = (1 + i\alpha) \left[\int_0^1 \psi_k N r dr \right] E_k + F_k(t, \tau), \quad k = 1, 2, \tag{8}$$

$$T \frac{\partial N}{\partial t} = d_f \frac{1}{r} \frac{\partial}{\partial r} \left(r \left(\frac{\partial N}{\partial r} \right) \right) - N + J - \sum_{k=1,2} \left(\left(1 + 2 \int_0^1 \psi_k N r dr \right) \psi_k |E_k|^2 \right) \tag{9}$$

for the evolution of the two complex fields $E_1(t)$ and $E_2(t)$ and the real spatial carrier population $N(r, t)$. The fields E_1 and E_2 are associated with the modal profiles $\psi_1(r) \equiv \psi_{01}(r)$ and $\psi_2(r) \equiv \psi_{02}(r)$ of the LP_{01} and LP_{02} modes. The profiles ψ_1 and ψ_2 are shown in Figs. 2(a1) and (a2), and the projections of LP_{01} and LP_{02}, onto the E_1 and E_2 planes in Figs. 2(b1) and (b2), respectively.

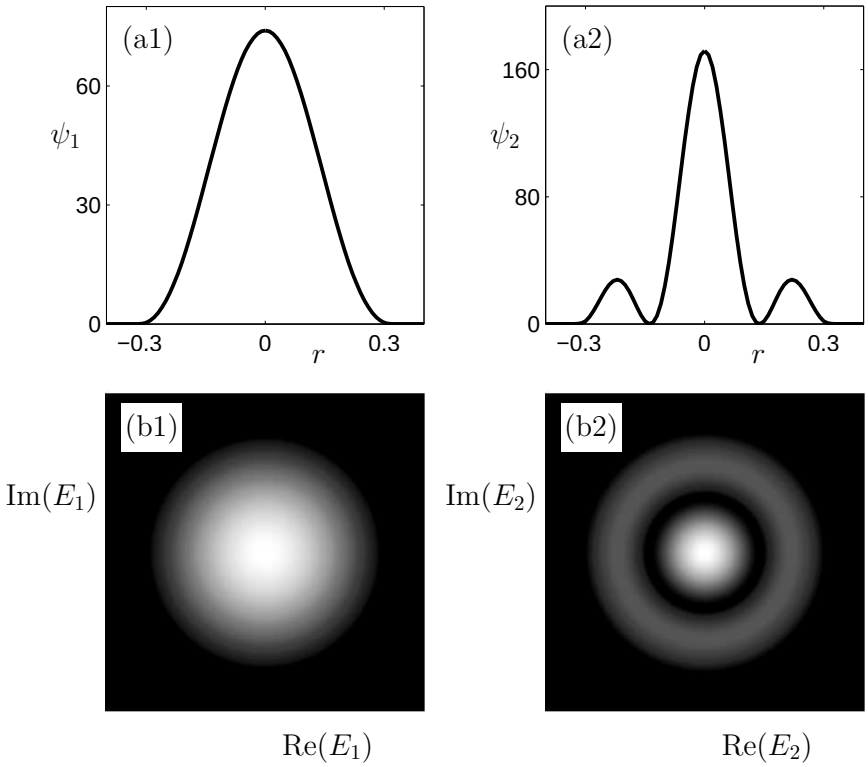

Fig. 2. The profiles ψ_1 (a1) and ψ_2 (a2) of the two basic modes LP_{01} and LP_{02}, and their projections onto the E_1 (b1) and E_2 planes (b2).

The integral terms in Eqs. (8) and (9) measure the overlap between the modal profiles and the carrier distribution.

Dimensionless parameters are the linewidth enhancement factor α, the diffusion coefficient d_f, and the ratio T between the carrier lifetime and the photon decay rate. We model the spatial pump $J(r)$ as

$$J(r) = \frac{(J_{\max}(r) - J_{\min}(r))}{2}(1 + \mathrm{erf}(2\sqrt{a}(-r + w_b))) + J_{\min}(r), \tag{10}$$

where $J_{\max}$ and $J_{\min}$ represent the values of the injection current (pump) when above the core and cladding regions, respectively. (In our formulation $J_{\min} = 0$.) The 'drop-off' of the pump between the core and cladding regions is modeled by the standard error function `erf`, as implemented in `Matlab`, so that the pump profile resembles a 'top-hat'. Furthermore, w_b defines the radius of the core region and a is a drop-off rate of the pump over the cladding region. The profile of the injection current directly affects the carrier concentration; see Refs. [20] and [24, Sec. 6.2.2]. We have chosen the profile (10) such that the current density is concentrated inside the core region, with weak confinement of the current inside the cladding layer. Other injection current profiles may include, for example, a circular-ring contact which excites higher order optical

modes [12] in the carrier profile. Conversely, one may consider a small disk contact focused on the center of the core, so that only the central, fundamental LP_{01} mode is excited [21].

We introduce the feedback functions $F_k(t,\tau)$ $(k = 1, 2)$ in Eq. (8) in the generalized form

$$F_1(t,\tau) = e^{iC_{p,1}}\kappa_1 \left[\eta_1 E_1(t-\tau) + e^{i\Delta C_p}(1-\eta_1)E_2(t-\tau)\right],$$

$$F_2(t,\tau) = e^{iC_{p,2}}\kappa_2 \left[e^{-i\Delta C_p}(1-\eta_2)E_1(t-\tau) + \eta_2 E_2(t-\tau)\right].$$

In the above formulation, κ_k represents a total feedback strength (comparable to the standard COF feedback strength parameter) and $C_{p,k}$ is the total feedback phase. As with COF, $C_{p,k}$ can be treated as a separate parameter that is independent of τ; it can be varied, for example, by adjusting the length of the external cavity on the scale of the optical wavelength. Furthermore, ΔC_p represents a difference between the optical frequencies of the two cavity modes in the absence of feedback. Finally, the parameters η_1 and η_2 represent the degree of self- versus cross-feedback that E_1 and E_2 receive from each other. Varying continuously between zero and one, η_1 and η_2 are homotopy parameters between the two extremes of only self-feedback and only cross-feedback in the respective LP mode.

We now make the simplifying modeling assumption that both LP modes, which would be expected to be very close in frequency in any VCSEL, actually have the same optical frequency, meaning that $\Delta C_p = 0$. Therefore, the feedback phase is the same for both LP modes, that is, $C_{p,1} = C_{p,2} \equiv C_p$, so that we are dealing with a single feedback phase in the model. We remark that the effect of small frequency differences of 0.2 nm between three LP_{0n} modes is briefly discussed in Ref. [18], where the conclusion is that the observed dynamics are robust under this perturbation of the model. Since we are considering here the continuous change from both electric fields receiving only self-feedback to both receiving only cross-feedback, we introduce the single feedback rate $\kappa = \kappa_1 = \kappa_2$ and the single homotopy parameter $\eta \in [0, 1]$ by $\eta = \eta_1 = \eta_2$. The general feedback terms then simplify to

$$F_1(t,\tau) = e^{iC_p}\kappa \left[\eta E_1(t-\tau) + (1-\eta)E_2(t-\tau)\right], \tag{11}$$

$$F_2(t,\tau) = e^{iC_p}\kappa \left[(1-\eta)E_1(t-\tau) + \eta E_2(t-\tau)\right]. \tag{12}$$

In our bifurcation study we adopt realistic parameter values, namely $\alpha = 3.0$, $d_f = 0.05$, $T = 750.0$, $a = 75$, $w_b = 0.3$, $J_{\min} = 0.0$ and $J_{\max} = 2.0$. Note that the value of pump current was chosen well (approximately four times) above threshold so that the system is lasing. Moreover, we fix the dimensionless

propagation time between the VCSEL and the external reflector at $\tau = 500$, which corresponds to a physical distance of approximately ten centimeters.

The feedback rate $\kappa \geq 0$, the 2π-periodic feedback phase C_p and the homotopy parameter $\eta \in [0, 1]$ are free parameters in our bifurcation study. Specifically, we study how ECM-components (for fixed κ and varying C_p) and branches of ECMs (for fixed C_p and varying κ) depend on the amount of self- versus cross-feedback as represented by η. We consider in detail the weak feedback regime where $\kappa \in [0, 0.006]$, and also discuss briefly the larger feedback range $\kappa \in [0, 0.5]$. The upper limits of $\kappa = 0.006$ and $\kappa = 0.5$ correspond to upper limits on the physical external reflectivity r_{ext} of the order of magnitude $r_{\text{ext}} \sim 10^{-5}$ (weak feedback) and $r_{\text{ext}} \sim 10^{-1}$, respectively [18]. The feedback rate κ is impossible to determine directly in an experiment. However, by using κ as a bifurcation parameter and comparing theoretical and experimental results (especially the number of ECMs and their dependence on C_p) one may obtain a good indication of the actual experimental feedback rate.

Apart from the obvious symmetry $C_p \to C_p + 2n\pi, n \in \mathbb{Z}$ of the feedback phase parameter C_p, Eqs. (8)–(12) have a continuous S^1-symmetry, which is a well-known feature of models describing semiconductor lasers subject to coherent optical feedback [7]. Namely, the transformation

$$(E_1, E_2, N) \to (cE_1, cE_2, N) \tag{13}$$

where $\{c \in \mathbb{C} : \|c\| = 1\}$ leaves the equations invariant. In other words, rotating both complex fields E_1 and E_2 of a solution over any angle $b \in [0, 2\pi]$ yields another solution of Eqs. (8)–(12).

3.1 Numerical implementation of the system

We discretize Eq. (9) with a second-order finite difference scheme on a uniform mesh. We consider 100 intervals, over half of the transverse length $r \in [0, 1]$; that is, over the rescaled radius of the VCSEL. At $r = 0$ we impose zero Neumann boundary conditions, and at $r = 1$ zero Dirichlet boundary conditions; that is, $\partial N/\partial r = 0$ at $r = 0$, and $N = 0$ at $r = 1$, respectively. The resulting DDE system has size 105, where the real and imaginary parts of E_1 and E_2 are real scalars, and N is a real vector of length 101. (The spatial variables ψ and J also have length 101.) The overlap integrals are solved by using the trapezoidal numerical integration method. Because of its size, even simulated results obtained from a direct numerical integration of the discretized Eqs. (8)–(12) are very time-consuming.

In this paper we employ numerical continuation techniques that allow us to

find and follow, in parameters, branches of steady state solutions irrespective of their stability. Specifically, we use the continuation package DDE-BIFTOOL [1] for the numerical bifurcation analysis of DDEs. This package has been used with good success for determining the stability of the external modes found in feedback lasers described by systems of DDEs of small size (of, say, below six equations), for example, the COF [5], FOF [2] and mutually-coupled lasers [3].

By contrast, the bifurcation analysis of the discretization of Eqs. (8)–(12) is quite challenging due to the large problem size. In particular, the calculation of stability information is computationally very expensive for large-scale systems such as the VCSEL model considered here. Specifically, the time taken for the stability computation of a single ECM in our 106-dimensional model with the standard DDE-BIFTOOL routines was approximately 7 minutes on a 3.4 GHz Intel Xeon processor. As each branch of ECMs consists of hundreds of points (which are needed for an accurate identification of the bifurcation points), obtaining the stability information presented in Figs. 9 and 10 below has been a costly computational exercise that presents the present state-of-the-art.

As with other systems with an S^1-symmetry such as (13), one needs to ensure in the numerical continuation that an isolated solution is considered. To this end, we move to a rotating frame with frequency b and impose an extra condition [5], that is,

$$E(t) = A(t)\exp(ibt) \quad \text{with} \quad \mathrm{Im}(A_s) = 0, \tag{14}$$

where Im denotes the imaginary part of the steady state A_s. Thus, a single solution of Eqs. (8)–(12) is isolated. This extra scalar condition adds a further row to the governing system when computing steady state solutions, resulting in a system of 106 equations.

4 External cavity mode structure

As is the case for the COF [16], FOF [4] and mutually-coupled lasers [3], the most basic solutions of Eqs. (8) to (12) have constant intensity, inversion and frequency. In analogy to the COF case, we refer to them as *external cavity modes* (ECMs). They are of the form,

$$(E_1(t), E_2(t), N(r,t)) = (R_1 e^{i\omega_s t}, R_2 e^{i\omega_s t + i\Phi}, N_s(r)), \tag{15}$$

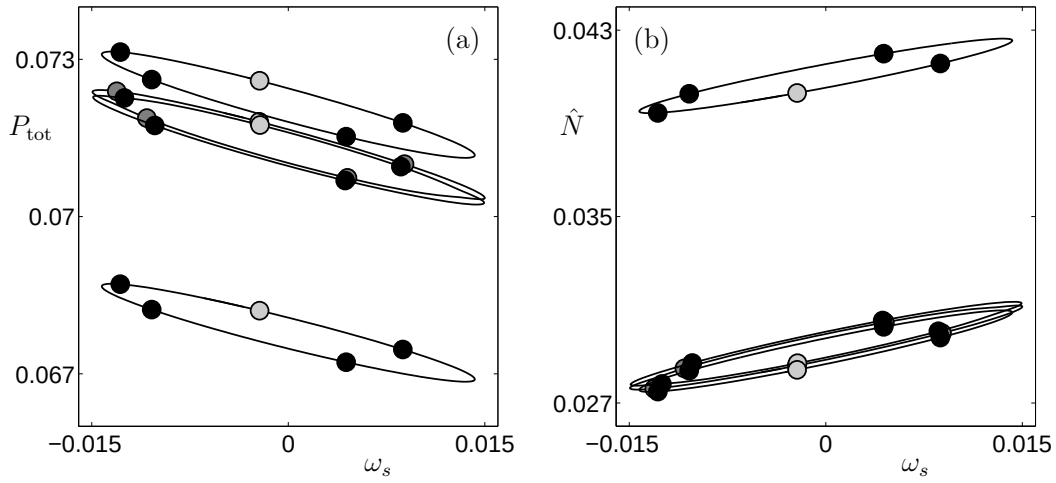

Fig. 3. ECM-components for $\eta = 0.9$ and $\kappa = 0.005$; ECMs are shown as large dots for $C_p = 2n\pi$, $n \in \mathbb{Z}$.

where R_1, R_2, ω_s, Φ, $N_s(r) \in \mathbb{R}$. Physically, $R_1 = |E_1|$ and $R_2 = |E_2|$ are constant amplitudes of the two electric fields under consideration, ω_s is the frequency of the output light, Φ is a fixed phase difference, and $N_s(r)$ is a fixed level of inversion (the number of electron hole pairs from which both fields feed) in both space and time. The individual field intensities are given as $P_1 = R_1^2$ and $P_2 = R_2^2$, and the total field intensity as $P_{\rm tot} = P_1 + P_2 = |E_1|^2 + |E_2|^2$.

Due to the spatial nature of the problem, we cannot simply plug Eq. (15) into Eqs. (8)–(12) and obtain expressions for the ECMs (a technique used in other, non-spatially extended laser systems, as described by the Lang-Kobayashi equations [9], where the first step is to find the ECM frequencies as solutions of a transcendental equation; see, for example, Ref. [4]). Instead, we turn to numerical continuation techniques. After obtaining a starting ECM solution, for example, from numerical simulation, we compute branches of ECMs of Eqs. (8)–(12) as a function of selected parameters. As is the case for the ECMs of the COF laser and the external filtered modes (EFMs) of the FOF laser, we find that the ECMs of our VCSEL model lie on closed curves that we refer to as *ECM-components*. They are computed with the feedback phase C_p as the continuation parameter; note that the extra parameter b is always free, in order to balance the extra condition (14), ensuring that we follow the same solution during continuation. Specifically, C_p parametrizes the ECM-components, while b gives the ECM frequency ω_s.

Figure 3 shows the ECM-components of Eqs. (8)–(12) for a weak feedback strength of $\kappa = 0.005$ and predominantly self-feedback, namely for $\eta = 0.9$. This value of η was chosen because, as we shall see in the following sections, it provides a quantitatively generic ECM structure for the low, through to the intermediate, cross-feedback regime. Also plotted are the ECMs (large dots) for $C_p = 2n\pi$, $n \in \mathbb{Z}$; see Eqs. (11) and (12). As C_p is varied, the ECMs

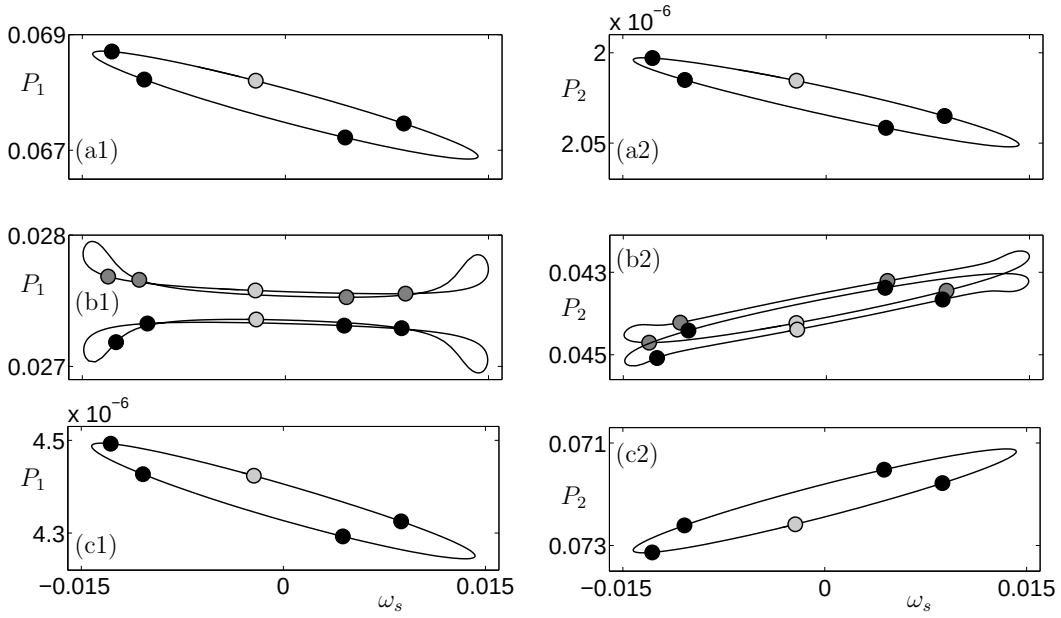

Fig. 4. Contributions of E_1 and E_2 to the ECM-components for $\eta = 0.9$ and $\kappa = 0.005$; ECMs are shown as large dots for $C_p = 2n\pi$, $n \in \mathbb{Z}$.

move along the ECM-components. A C_p-variation of 2π moves one ECM to the initial position of its closest neighbor. In our model, increasing C_p moves the ECMs from right to left along an ECM-component. For certain values of C_p, pairs of ECMs are created and lost in saddle-node bifurcations near the right and left-most limits of each ECM-component, respectively.

Figure 3 shows the ECM-components in the (ω_s, P_{tot})-plane and in the (ω_s, $\hat{N}_s$)-plane, respectively, where $\hat{N}_s$ represents the mean value of $N_s(r)$ over the spatial distance $r \in [0, 1]$. A first conclusion is that we find twenty ECMs that lie on four ECM-components. Note that the lower ECM-component in Fig. 3(a), for low values of P_{tot}, corresponds to the upper ECM-component in Fig. 3(b), for high values of $\hat{N}$. Likewise, the upper ECM-components in Fig. 3(a) correspond to the lower ECM-components in Fig. 3(b). This situation is quite different from a single-mode COF laser as modeled by the Lang-Kobayashi equations. In which the ECMs are known to lie on a single closed curve, namely an ellipse in the (ω_s, $\hat{N}_s$)-plane [16]. However, we note that, in both the (ω_s, P_{tot})-plane and in the (ω_s, $\hat{N}_s$)-plane, the ECM-components of Eqs. (8)–(12) have a similar elliptical shape as the ECMs ellipse of the COF laser. The number of ECM-components we find is also in contrast with other laser systems with coherent optical feedback. Namely, for the FOF laser the corresponding external filtered modes (EFMs) lie on either one or two closed curves, called *EFM-components* [4], and the compound laser modes (CLMs) of mutually-coupled lasers lie on two or three closed curves [3].

We now address the question of how the individual spatial modes contribute to the total intensity. This is shown in Fig. 4, where the two columns depict

the different ECM-components in the (ω_s, P_1)-plane and in the (ω_s, P_2)-plane, respectively. Specifically, the ECM-components in Figs. 4(a1) and (a2) correspond to the lowermost ECM-component in Fig. 3(a), the ECM-components in Figs. 4(b1) and (b2) to the innermost ECM-components in Fig. 3(a), and the ECM-components in Figs. 4(c1) and (c2) to the uppermost ECM-component in Fig. 3(a). To highlight the correspondence between the two columns of Fig. 4, P_1 decreases from (a1) to (c1), while P_2 increases from (a2) to (c2).

From considering the intensity levels of the two spatial modes, it can be seen that the ECM-component in Fig. 4, row (a), corresponds to solutions in which nearly all of the total intensity comes from E_1, that is, from the LP_{01} mode. Conversely, the ECM-components in row (c) correspond to solutions in which nearly all of the total intensity comes from E_2, that is, from the LP_{02} mode. Even when split into their P_1 and P_2 components, these ECM-components are again elliptical. This is not the case for the two intermediate ECM-components shown in row (b). Clearly these ECM-components, for which the field intensities P_1 and P_2 both contribute significantly to $P_{\rm tot}$, are no longer elliptical. Nevertheless, the ECM-component of the total field intensity (shown in Fig. 3(a)) is still elliptical.

5 Effect of feedback strength κ

In this section we follow branches of ECMs as the feedback strength κ is varied. The two columns of Fig. 5 show branches of ECMs in the (κ, P_1)-plane and in the the (κ, P_2)-plane, respectively. Again, we plot P_1 decreasing and P_2 increasing so that the solutions in panels (a1) to (c1) correspond to those in panels (a2) to (c2). These ECM branches are continued from (and correspond to) the ECMs for $\kappa = 0.005$ that are plotted as large dots in Fig. 4, where the respective gray-scales of the branches and the ECMs agree. The branches in rows (a) and (c) of Fig. 5 correspond to a dominant electric field E_1 associated with the LP_{01} mode, and a dominant E_2 associated with the LP_{02} mode, respectively. Similar solutions are also found in mutually-coupled lasers [3], where one laser may be 'on' while the other is 'off'. Furthermore, we have intermediate branches in Fig. 5(b) where both electric fields, that is, both spatial modes, contribute to the total intensity.

Our first observation is that, unlike for the COF and FOF lasers, we find more than one ECM for $\kappa = 0$. In fact, we find three ECMs (the end points of the light gray branches in Fig. 5). Namely, one ECM that is dominated by E_1 in row (a), one intermediate ECM in row (b), and one ECM that is dominated by E_2 in row (c). As κ is increased, the intermediate ECM for $\kappa = 0$ in Fig. 5(b) splits up into a pair of (light gray) ECM branches. Furthermore, additional branches of ECMs are born. Like for other feedback laser systems,

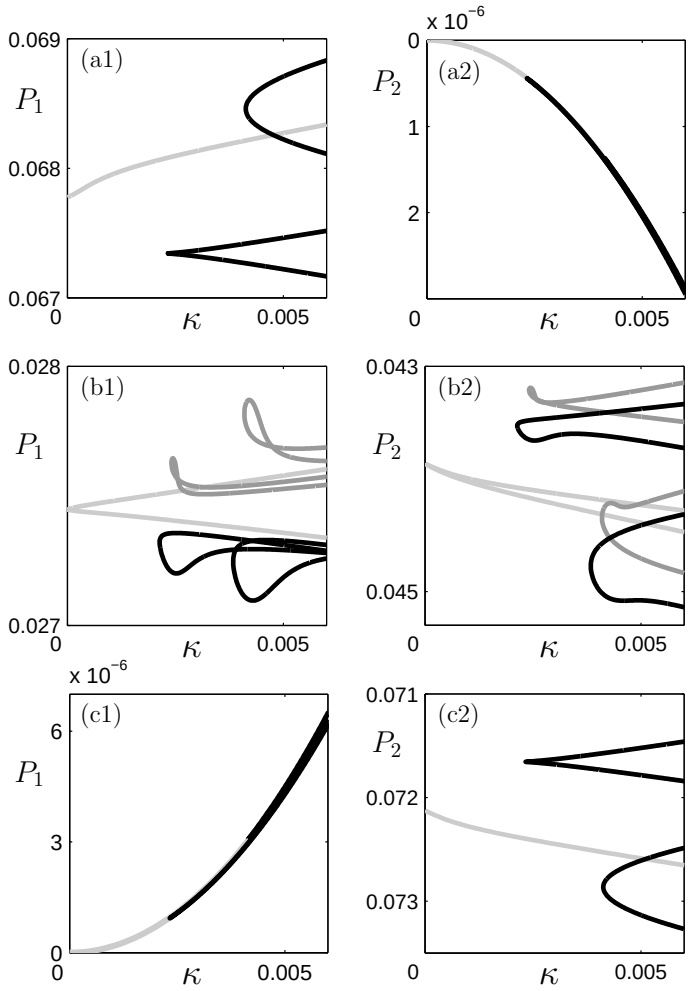

Fig. 5. Local ECM branches as a function of the feedback strength κ; for $C_p = 0$ and $\eta = 0.9$.

it is clear from their shape that new ECMs are born in pairs in saddle-node bifurcations. Again, the gray scale of the branches corresponds to that of the ECMs in Fig. 4. For the dominating E_1 and E_2 fields in Figs. 5(a2) and (c1) the two bifurcating ECM branches are nearly indistinguishable from one another, as are their leftmost turning points. For $\kappa = 0.005$ one finds five solutions in rows (a) and (c), as well as the ten solutions in row (b). Together they account for the twenty ECMs that are identified in Figs. 3 and 4.

As for the ECM-components shown in Figs. 3 and 4, we find that the different ECMs contribute differently to the total intensity P_{tot}. Namely, the E_1- or E_2-dominated ECM branches in Figs. 5(a) and (c) are much like those for other single mode lasers with optical feedback, while the ECM branches with significant contributions from E_1 and E_2 in Fig. 5(b) have a peculiar shape. However, we note that the shapes of all ECM branches in the (κ, P_{tot})-plane (not shown) are very similar that for the COF laser; see already Fig. 7(a). Overall, the picture of the individual intensity contributions of the ECM branches in

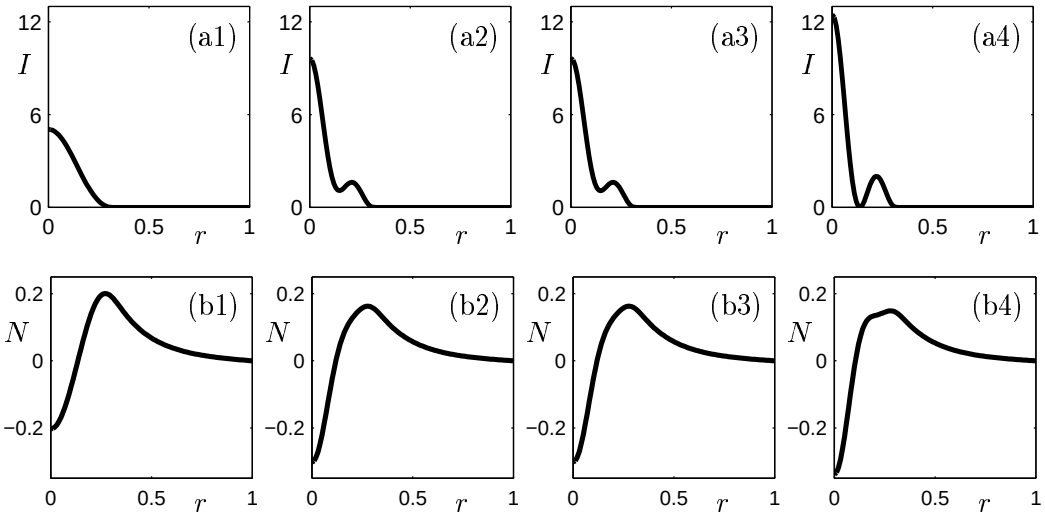

Fig. 6. Radial profiles of coexisting ECMS for fixed $\kappa = 0.005$, $C_p = 0$ and $\eta = 0.005$; shown are a measure of the total electric field intensity $I = \psi_1 P_1 + \psi_2 P_2$ in panels (a1) to (a4), and the inversion distribution N in panels (b1) to (b4).

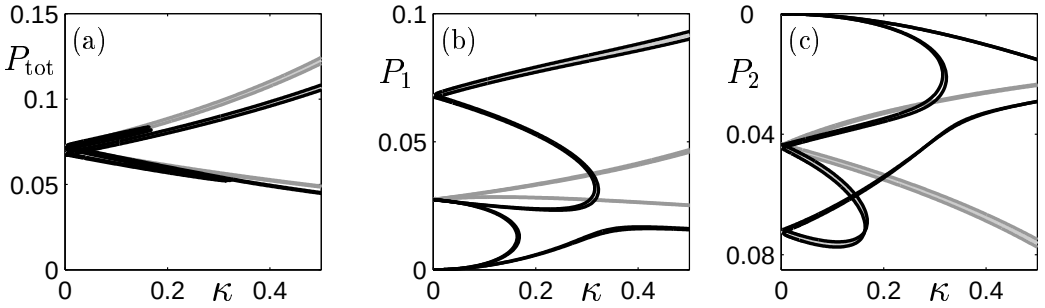

Fig. 7. Branches of ECMs for $\kappa \in [0, 0.5]$, $C_p = 0$ and $\eta = 0.9$.

the (κ, P_1)- and the (κ, P_2)-plane emerges as a characteristic feature of the two-mode VCSEL with the novel form of cross-feedback considered here.

To give an idea of the spatial nature of the different ECMs, Fig. 6 shows the radial profiles of their total spatial electric field intensity $I = \psi_1 P_1 + \psi_2 P_2$ in panels (a1) to (a4), and their inversion distribution $N(r)$ in panels (b1) to (b4). One can envisage the full three-dimensional intensity and inversion profiles simply by rotating these radial profiles around the line $r = 0$. The profiles shown are of the four ECMs on the light gray branches of Fig. 5 for $\kappa = 0.005$. Specifically, Fig. 6(a1)/(b1) is for the E_1-dominated ECM on the light gray ECM branch in Fig. 5(a1), Figs. 6(a2)/(b2) and (a3)/(b3) are for the two intermediate light gray ECM branches in Fig. 5(b), and Fig. 6(a4)/(b4) is for the E_2-dominated light gray ECM branch in Figs. 5(c). Note the effect of spatial-hole burning in the inversion distributions.

Finally, Fig. 7 shows the continuation to higher values of κ of the ECM branches that were identified in Fig. 5. As can be seen, at these higher val-

ues of κ the ECM branches form connections. Specifically, the black branches born in the saddle-node bifurcations in Fig. 5, row (a), connect with the black branches born in the first saddle-node bifurcations in Fig. 5, rows (b) and (c). In fact, many of the local branches, in which one of the fields dominates, were found from the continuation of a single, stable ECM for which both fields contribute to the total intensity. This shows that, in order to fully understand the structure of the ECMs, one must look over this larger κ-range. Again we find that the ECM branches corresponding to the individual intensities P_1 and P_2 (Figs. 7(b) and (c), respectively) are more complicated than their sum P_{tot} in Fig. 7(a). Furthermore, at higher values of κ the black branches are clearly seen to have right-most turning points, which correspond to the disappearance of ECMs in saddle-node bifurcations as κ is increased. Specifically, these occur at $\kappa \approx 0.17$ and $\kappa \approx 0.32$. Further details of the ECM branches for these higher values of κ are beyond the scope of this study, which concentrates on the more physically relevant weak feedback regime.

6 Effect of the cross-coupling parameter η

We now investigate what effect the cross-coupling parameter η has on the ECM structure of our VCSEL model. Specifically, we go from the *degenerate case* in which both electric fields, E_1 and E_2, only receive feedback from themselves (Eqs. (11) and (12) with $\eta = 1$), to the case when both fields receive feedback only from each other ($\eta = 0$); in other words, we consider the entire transition from purely self-feedback to purely cross-feedback. Throughout this section, we first compute initial ECMs, and the ECM-components on which they lie, for a weak feedback strength of $\kappa = 0.005$. We then compute the two branches, for which both fields contribute to the total intensity in the weak feedback regime ($\kappa \in [0,\, 0.006]$), where we identify changes in the structure. Furthermore, in this section we also show stability information along these branches.

6.1 Intermediate ECM-components as a function of η

For a weak feedback strength of $\kappa = 0.005$, we now examine changes in the shape of the ECM-components as η is varied. Specifically, we investigate changes to the intermediate ECM-components, for which both fields E_1 and E_2 contribute to the total intensity P_{tot}; that is, we consider the ECM-components shown in Figs. 4(b1) and (b2). Figures 8(a) to (i) show ECM-components, in the (ω_s, P_1)-plane, for $\eta = 1.0$, 0.99, 0.9, 0.6, 0.4, 0.3, 0.2, 0.1 and 0.0, respectively. Also shown, as large dots, are the ECMs for $C_p = 2n\pi$, $n \in \mathbb{Z}$. Figure 8(a) shows five ECMs lying on a single ECM-component for the case $\eta = 1$. As η is decreased, two separate ECM-components emerge. Like-

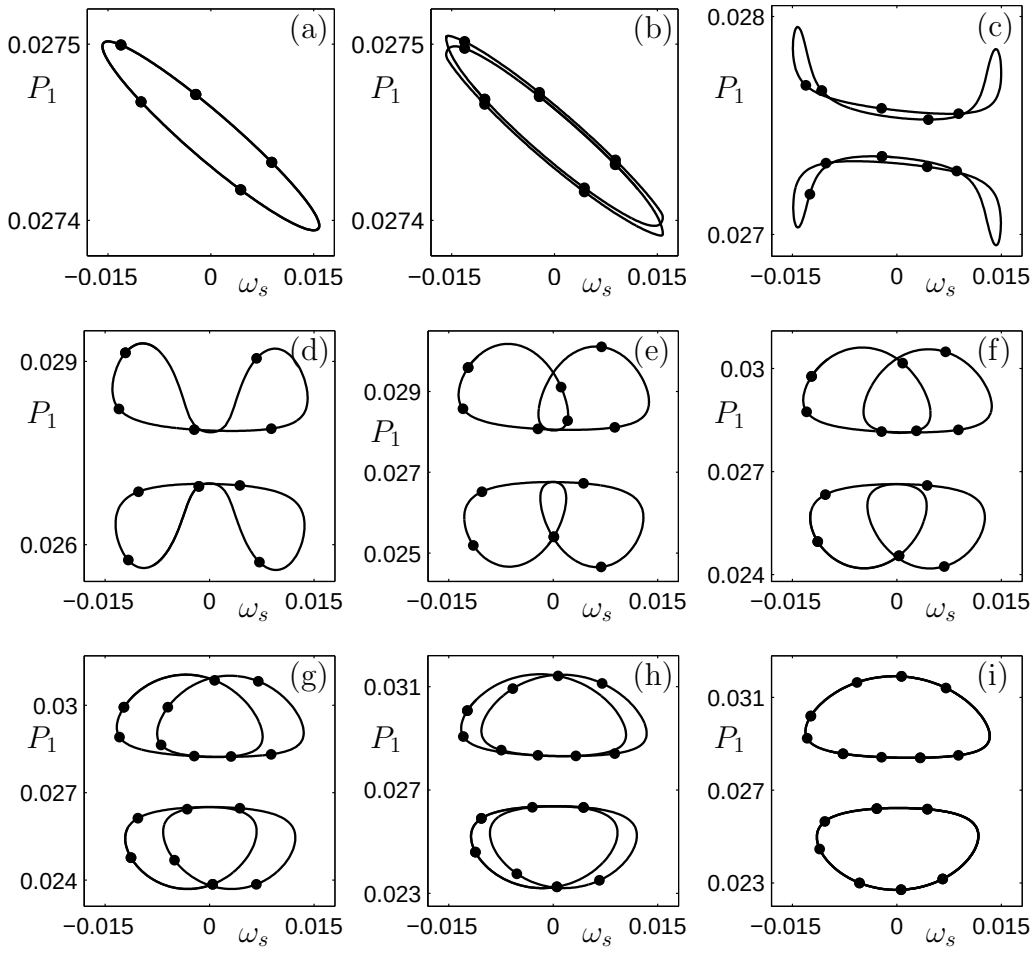

Fig. 8. Local ECM-components for decreasing η. From (a) to (h), η takes the values 1.0, 0.99, 0.9, 0.6, 0.4, 0.3, 0.2, 0.1 and 0.0, respectively; for fixed $\kappa = 0.005$.

wise, the number of ECMs, for fixed C_p, doubles; see Fig. 8(b) for $\eta = 0.99$. The conclusion is that for $\eta = 1$ the ECM branch is actually *double-covered*; this degenerate situation is similar to the case of two mutually delay-coupled lasers with the exact same lasing frequency [3]. As η is decreased further, the ECM-components move away from an elliptical shape; see Figs. 8(c) and 8(d) for $\eta = 0.9$ and 0.6, respectively. This is the generic situation, for a small to intermediate amount of cross-feedback, where one finds five ECMs on each component. Furthermore, each ECM-component is starting to fold over onto itself as η is decreased; see Figs. 8(e) and (f). This process continues and each ECM-component 'coils up'; Figs. 8(g) and (h). Until, for $\eta = 0$, the two separate ECM-components have completely folded over onto themselves; that is, they are again double-covered; see Fig. 8(i). However, now, for the case of purely cross-feedback, we have two clearly separated, double-covered ECM-components on which the ECMs *appear* to be separated by $C_p \approx \pi$.

6.2 Dependence of ECM branches on η

We now consider how the structure of the intermediate ECM branches (as a function of the feedback strength κ) is affected by the homotopy parameter η.

Figures 9 and 10 show these ECM branches in the (κ, P_1) and (κ, P_2)-planes, respectively, for values of η ranging from $\eta = 1.0$ (a) to $\eta = 0.0$ (i). Importantly, we now also show the stability information along the branches. Namely, stable ECMs are shown as black curves and unstable ones as gray curves. Saddle-node bifurcations, corresponding to a real eigenvalue passing through zero, are indicated by crosses ($\times$). As before, these bifurcations are folds with respect to the parameter κ and lead to the creation of pairs of branches of ECMs as κ is increased. Hopf bifurcations, corresponding to a pair of complex eigenvalues crossing the imaginary axis, are indicated by stars ($*$). They lead to periodic solutions, which in turn may undergo further bifurcations leading to more complex dynamics.

Determining the stability of the external modes found in feedback lasers described by systems of DDEs of small size (of, say, below six equations), for example, the COF [5], FOF [2] and mutually-coupled lasers [3], can now be done routinely. By contrast, the calculation of stability information is computationally very expensive for large-scale systems such as the discretization of the DPDE VCSEL model Eqs. (8) to (12). As detailed earlier, the time taken for the stability computation of a single ECM in our 106-dimensional model with the standard DDE-BIFTOOL routines was approximately 7 minutes on a 3.4 GHz Intel Xeon processor. As each branch of ECMs consists of hundreds of points (which are needed for an accurate identification of the bifurcation points), obtaining Figs. 9 and 10 has been a costly computational exercise that presents the present state-of-the-art. We remark that it is an important topic for future research to improve the efficiency of stability computations, either with methods as outlined in Ref. [23], or possibly by reducing the size of the VCSEL model, for example, with techniques as first introduced in Ref. [14].

We first discuss some common features of the panels of Figs. 9 and 10. First of all, one branch of stable ECMs is born at $\kappa = 0$ and is destabilized in a Hopf bifurcation at $\kappa \approx 0.005$. This Hopf bifurcation moves to slightly higher values of κ as η is decreased; see Figs. 9 and 10, (a) to (i). Furthermore, the stability analysis shows that for all values of η we have a coexistence of stable ECMs for certain ranges of κ. In the physical context, the system will lase in one of the stable ECMs as determined by the initial condition. Furthermore, perturbations, such as noise, may cause the system to jump from one stable state to another.

We now consider the changes to the intermediate ECM branches as η is de-

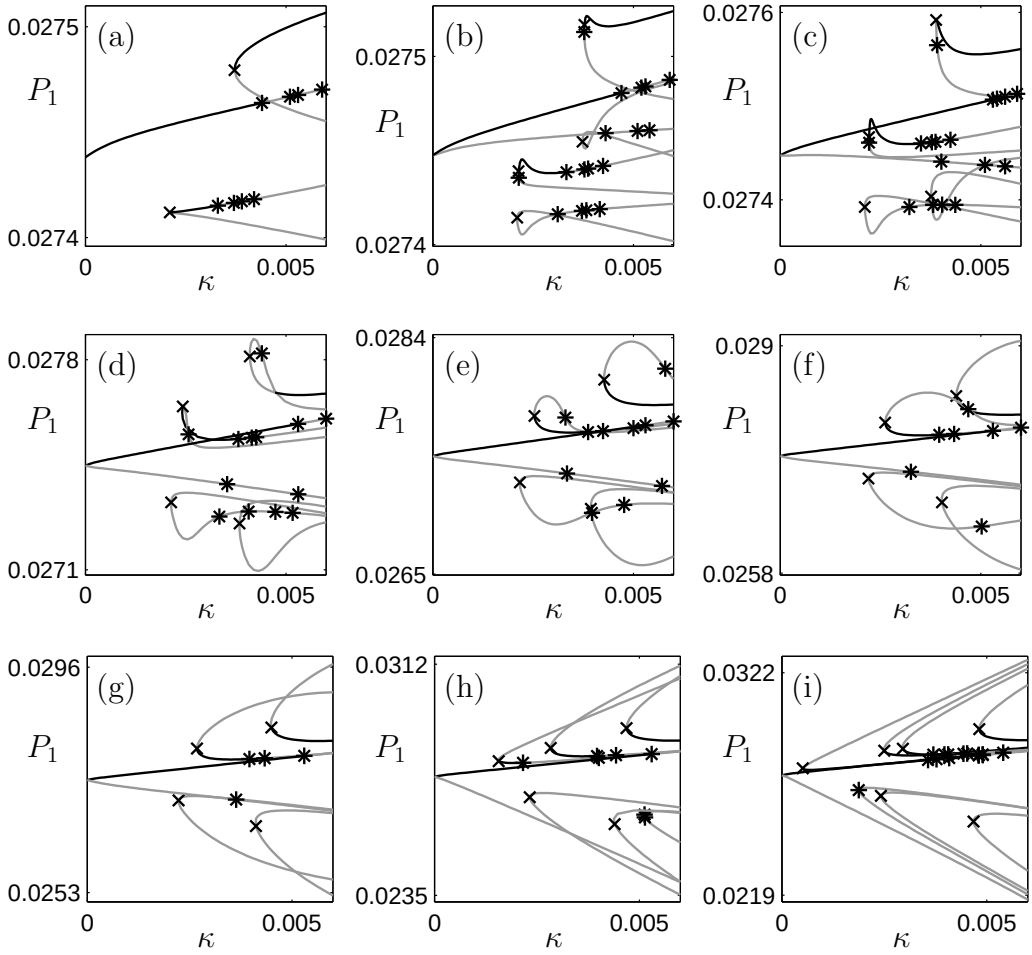

Fig. 9. Local branches of ECMs in the (κ, P_1)-plane. From (a) to (i), η takes the values 1.0, 0.99, 0.97, 0.9, 0.8, 0.7, 0.6, 0.3 and 0.0, respectively. Stable ECMs are drawn as black curves and unstable ones as gray curves; saddle-node bifurcations are indicated by crosses ($\times$) and Hopf bifurcations by stars ($*$).

creased. Note that there is little local change in the structure of the other local branches, that is, those identified in Figs. 5(a1) and (a2), and (c1) and (c2); these solutions are unstable for all η. Our starting point is the degenerate case of purely self-feedback, $\eta = 1$, as shown in Figs. 9(a) and 10(a). Here we find three branches and, hence, five (local) ECMs at $\kappa = 0.005$; namely the ECMs shown in Fig. 8(a). The branches in Fig. 9(a) are shown to have a similar shape to those shown in Fig. 10(a). In fact, at the special value of $\eta = 1$, they resemble the ECM branches found in the COF and FOF lasers. As η is decreased, the three local branches turn into six branches; see Figs. 9(b) and 10(b) for $\eta = 0.99$. Thus, we again find ten local ECMs at $\kappa = 0.005$; compare with Figs. 4 and 5, (a2) and (b2), and Figs. 8(a) and (b). Like for the ECM-component shown in Fig. 8(a), the three branches found for $\eta = 1$ are double covered. In the process, the number of saddle-node bifurcations doubles from two to four. This can be seen most clearly in the unfolding of the branches

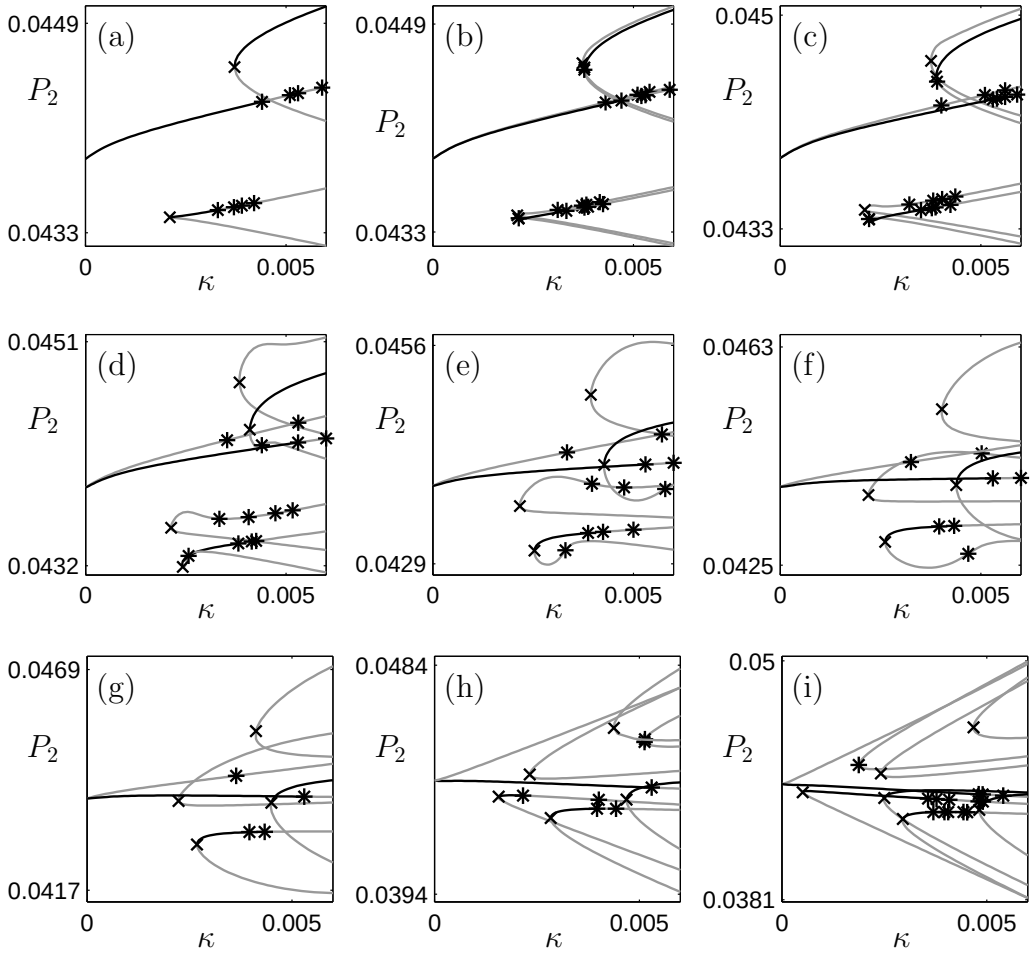

Fig. 10. Local branches of ECMs in the (κ, P_2)-plane. From (a) to (i), η takes the values 1.0, 0.99, 0.97, 0.9, 0.8, 0.7, 0.6, 0.3 and 0.0, respectively. Stable ECMs are drawn as black curves and unstable ones as gray curves; saddle-node bifurcations are indicated by crosses ($\times$) and Hopf bifurcations by stars ($*$).

associated with the E_1-field; see Fig. 9(b). Importantly, in the transition to $\eta < 1$ only one of the two unfolded branches 'inherits' the stability region found for $\eta = 1$; namely, the branch at higher values of P_1 and lower values of P_2; see Figs. 9(b) and 10(b), respectively.

Decreasing η further, as in Figs. 9(c)–(f), and 10(c)–(f), one finds that the ECM branch structure associated with the E_1-field (Fig. 9) increasingly drifts from the degenerate case. Furthermore, the branch containing stable ECMs that moved upwards from Fig. 9(a) to (b) (and downwards from Fig. 10(a) to (b)) continues to do so as η is decreased. Likewise, an unstable branch, uncovered from the branch at the top of Fig. 9(a) moves downwards (and again upwards in Fig. 10) as η is decreased. A convergent ECM branch structure then starts to become apparent; see as an example Figs. 9(g) and 10(g), for $\eta = 0.6$.

However, Figs. 9(h) and 10(h) for $\eta = 0.3$ show a qualitative and quantitative change in the local ECM branch structure. Namely, two extra branches are shown to enter the region of $\kappa < 0.006$. These branches were continued from the extra ECMs revealed during the computation of Fig. 8, panels (e) to (g). Both branches have leftmost turning points, which are saddle-node bifurcations. The first to enter the weak feedback regime does so at high values of P_1 (low values of P_2) for $\eta \approx 0.429$ and moves to lower values of κ as η is decreased. In fact, for $\eta = 0.3$, Figs. 9(h) and 10(h) show it as the leftmost branch, born in a saddle-node bifurcation. Moreover, this branch is shown to contain stable ECMs. Hence, for increasingly lower values of η, we have a coexistence between stable ECMs at increasingly lower values of κ. The second additional branch in Figs. 9(h) and 10(h) enters $\kappa < 0.006$ for $\eta \approx 0.324$, namely at low values of P_1 (high values of P_2). This branch is the rightmost in Figs. 9(h) and 10(h), and it is always unstable. Finally, Figs. 9(i) and 10(i) show the ECM structure for $\eta = 0.0$, that is, for the purely cross-feedback case where the E_1-field receives feedback only from E_2, and vice versa. Figure 9(i) is approximately the mirror image of Fig. 10(i); the slight differences are due to the differing radial profiles of the respective fields E_1 and E_2. Moreover, one finds all stable ECMs on the branches at the top of Fig. 9(i); likewise, at the bottom of Fig. 10(i). Once more, an additional branch has entered $\kappa < 0.006$ at high values of P_1 (low values of P_2). This occurs at $\eta \approx 0.277$; see Figs. 8(f) to (g). Again, this branch contains stable ECMs, resulting in further multistability. Finally, we note that, the intensity ranges of the ECMs increases dramatically in Figs. 9 and 10 from panels (a) to (i). This has the consequence that for larger cross-coupling (smaller η) we expect larger power fluctuations in the dynamics, when the trajectory 'visits' these ECMs [6,22].

7 Conclusions

We have analyzed the external-cavity mode structure of a VCSEL with two spatial modes that is subject to optical feedback. Specifically, we have considered the influence of self- versus cross-coupling in the feedback field on the ECM structure of the system. A numerical bifurcation analysis revealed that the case of only self-feedback of the spatial modes is degenerate, because the ECMs are double-covered. This means that even very small cross-coupling doubles the number of ECMs. On the other hand, the ECM structure does not change qualitatively over a physically relevant range of feedback strength.

As is the case for other laser systems with optical feedback, the ECM structure underpins more complex dynamics of the VCSEL subject to feedback. Our stability results already revealed Hopf bifurcations that give rise to bifurcating stable periodic solutions, which in turn may bifurcate further. The stability analysis of the ECMs as presented here represents the present state-of-the-art

for the numerical bifurcation analysis of large systems of DDEs.

The numerical continuation of periodic solutions (corresponding to oscillations of the total intensity) and their stability in the form of Floquet multipliers is the next logical step. However, due to the large system size, the calculation of Floquet multipliers is prohibitively expensive with standard bifurcation software for delay equations. Therefore, it is an important topic for future research to improve the efficiency of stability computations, either with methods as outlined in Ref. [23], or possibly by reducing the size of the VCSEL model itself, for example, with techniques as first introduced in Ref. [14].

Finally, we note that the VCSEL model may be extended to include additional spatial modes of the VCSEL. An initial study has already shown that one must expect an increasingly rich ECM structure as more modes are considered. We remark that the addition of LP modes that are not rotationally symmetric makes it necessary to study a two-dimensional carrier distribution. This dramatically increases the system size after discretization of the PDE part. A bifurcation analysis of a wide-aperture VCSEL with many different spatial modes remains a considerable challenge.

References

[1] K. Engelborghs and D. Roose. On stability of LMS methods and characteristic roots of delay differential equations. *SIAM J. Numer. Anal.*, 40:629–650, 2002.

[2] H. Erzgräber, B. Krauskopf, and D. Lenstra. Bifurcation analysis of a semiconductor laser with filtered optical feedback. *SIAM J. Applied Dynamical Systems*, 6(1):1–28, 2007.

[3] H. Erzgräber, B. Krauskopf, and D. Lenstra. Compound laser modes of mutually delay-coupled lasers. *SIAM J. Applied Dynamical Systems*, 5(1):30–65, 2006.

[4] K. Green and B. Krauskopf. Mode structure of a semiconductor laser subject to filtered optical feedback. *Opt. Commun.*, 258:243–255, 2006.

[5] B. Haegeman, K. Engelborghs, D. Roose, D. Pieroux, and T. Erneux. Stability and rupture of bifurcation bridges in semiconductor lasers subject to optical feedback. *Phys. Rev. E*, 66(046216), 2002.

[6] T. Heil, I. Fischer, W. Elsäßer, B. Krauskopf, K. Green and A. Gavrielides. Delay dynamics of semiconductor lasers with short external cavities: Bifurcation scenarios and mechanisms. *Phys. Rev. E*, 67(066214), 2003.

[7] B. Krauskopf, G. H. M. Van Tartwijk, and G. R. Gray. Symmetry properties of lasers subject to optical feedback. *Opt. Commun.*, 177:347–353, 2000.

[8] B. Krauskopf. *Unlocking Dynamical Diversity: Optical Feedback Effects on Semiconductor Lasers*, chapter 5 Bifurcation Analysis of Lasers with Delay. Wiley, March 2005.

[9] R. Lang and K. Kobayashi. External optical feedback effects on semiconductor injection laser properties. *IEEE J. Quantum Electron.*, 16(3):347–355, 1980.

[10] J. Y. Law and C. P. Agrawal. Effect of optical feedback on static and dynamic characteristics of vertical-cavity surface-emitting lasers. *IEEE J. Quantum Electron*, 3:353–358, 1997.

[11] J. Y. Law and C. P. Agrawal. Nonlinear spatio-temporal dynamics due to transverse-mode competition in gain-switched microcavity semiconductor lasers. *Optics Commun.*, 138:95–98, 1997.

[12] J. Y. Law and C. P. Agrawal. Feedback-induced chaos and intensity-noise enhancement in vertical-cavity surface-emitting lasers. *J. Opt. Soc. Am. B*, 15(2):562–569, 1998.

[13] E. Mohammed, A. Alduino, T. Thomas, H. Braunisch, D. Lu, J. Heck, A. Liu, I. Young, B. Barnett, G. Vandentop, and R. Mooney. Optical interconnect system integration for ultra-short-reach applications. *Intel Technology Journal*, 8(2):115–127, 2004.

[14] K. Moriki, H. Nakahara, T. Hattori, and K. Iga. Single Transverse Mode Condition of Surface-Emitting Injection Lasers. *Elec. Commun. Japan*, 71(1):81–90, 1988.

[15] J. Martin-Regalado, S. Balle, M. San Miguel, A. Valle, and L. Pesquera. Polarization and transverse-mode selection in quantum-well vertical-cavity surface-emitting lasers: index- and gain-guided devices. *Quantum Semiclass. Opt.*, 9:713–736, 1997.

[16] T. Sano. Antimode dynamics and chaotic itinerancy in the coherence collapse of semiconductor lasers with optical feedback. *Phys. Rev. A*, 50(3):2719–2726, 1994.

[17] M. Sciamanna, T. Erneux, F. Rogister, O. Deparis, P. Mégret, and M. Blondel. Bifurcation bridges between external-cavity modes lead to polarization self-modulation in vertical-cavity surface-emitting lasers *Phys. Rev. A*, 65(041801), 2002.

[18] M. S. Torre, C. Masoller, and P. Mandel. Transverse-mode dynamics in vertical-cavity surface-emitting lasers with optical feedback. *Phys. Rev. A*, 66(053817), 2002.

[19] M. S. Torre, C. Masoller, P. Mandel, and K. A. Shore. Transverse-mode dynamics in directly modulated vertical-cavity surface-emitting lasers with optical feedback. *IEEE J. Quantum Electon.*, 40(6):620–628, 2004.

[20] A. Valle. Selection and modulation of high-order transverse modes in vertical-cavity surface-emitting lasers. *IEEE J. Quantum Electron.*, 34(10):1924–1932, 1998.

[21] A. Valle, J. Sarma, and K. A. Shore. Spatial holeburning effects on the dynamics of vertical cavity surface-emitting laser diodes. *IEEE J. Quantum Electron.*, 31(8):1423–1431, 1995.

[22] G. H. M. Van Tartwijk and A. M. Levine. Sisyphus effect in semiconductor lasers with optical feedback. *IEEE J. Quantum. Elec.*, 1(2):466–472, 1995.

[23] K. Verheyden, T. Luzyanina, and D. Roose. Efficient computation of characteristic roots of delay differential equations using lms methods. Technical Report TW-383, Department of Computer Science, K. U. Leuven, Belgium, 2004.

[24] S. F. Yu. *Analysis and Design of Vertical Cavity Surface Emitting Lasers*. John Wiley & Sons, 2003.